Pulsed ENDOR and ESEEM Study of [Bis(maleonitriledithiolato)nickel]$^{-}$: An Investigation into the Ligand Electronic Structure

Jennifer E. Huyett,[†] Suranjan B. Choudhury,[‡] David M. Eichhorn,[†,§] Peter A. Bryngelson,[‡] Michael J. Maroney,*[,‡] and Brian M. Hoffman*[,†]

Departments of Chemistry, Northwestern University, Evanston, Illinois 60208-3113, and University of Massachusetts, Amherst, Massachusetts 01003-4510

Received March 27, 1997

By a combination of Q-band pulsed ENDOR (electron nuclear double resonance) and X-band ESEEM (electron stimulated echo envelope modulation) techniques, we have determined the hyperfine tensors for ethylene (C1) and cyano (C2) carbons and N, of $[Ni(mnt)_2]^-$, along with the quadrupole tensor for nitrogen. These measurements give π electron spin densities of $\rho(C1) \sim 0.03$ in the C1 $2p_z$ orbital, $\rho(C2) < 0.003$, $\rho(N) \sim 0.01$, such that in total, ~0.15 of the spin resides on the ligand atoms C and N, while the rest resides in the NiS_4 core, giving $\rho(NiS_4^-) = 0.85$. These results are compared with extended Hückel and density functional (BLYP) MO calculations, as well as with Xα calculations reported earlier.

Introduction

Since the discovery in the mid-1970s that the hydrolytic enzyme urease contains a Ni,[1] the list of proteins and enzymes that specifically bind Ni has grown to include the group of redox enzymes comprising methyl coenzyme M reductase,[2] CO dehydrogenase,[3] and the majority of the hydrogenases. Because these enzymes catalyze two-electron redox processes and Ni coordinated by innocent ligands has only one common oxidation state (Ni(II)), the role of Ni as a redox center seemed counterintuitive. However, in each enzyme where Ni appears to be redox active, it is ligated by sulfur, which can participate in a redox process or in charge delocalization, as shown by studies on nickel dithiolates. In particular, in the case of CO-dehydrogenases and hydrogenases, EXAFS (extended X-ray absorption fine structure) analysis and crystal structures show that the Ni is ligated by cysteine thiolates,[4] and X-ray absorption spectroscopy (XAS) of the hydrogenase suggests that the redox changes are not localized on Ni.[5] To better understand the electronic structure of oxidized Ni thiolate complexes, we have used electron nuclear double resonance (ENDOR) and electron stimulated echo envelope modulation (ESEEM) spectroscopies to reexamine the electronic structure of planar bis(maleonitriledithiolato)nickel(III) ($[Ni(mnt)_2]^x$) (**1a**) and of bis((trifluoromethyl)ethylenedithiolato)nickel(III) ($[Ni(tfd)_2]^x$) (**1b**).

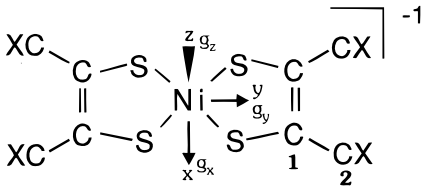

1a X = N
1b X = "F_3"

These compounds are of interest because they pass through several oxidation states ($x = 0, 1-, 2-$) without change in the metal coordination sphere and have a long history of studies done to determine whether the oxidation takes place at the ligand sulfurs ions or the metal ion. Specifically, EPR studies and molecular orbital calculations on the monoanion, $S = {}^1/_2$ state of $[Ni(mnt)_2]^-$ and $[Ni(tfd)_2]^-$ have tested whether the unpaired spin is located primarily on the ligand sulfur or on the metal ion, as Ni(III).[6−11] In a single-crystal EPR analysis, Maki et al.[6] assigned the rhombic **g** tensor of $[Ni(mnt)_2]^-$ to the molecular axes as shown in **1a** and interpreted it in terms of a d^7 compound with the unpaired electron residing in a d_{yz}-like SOMO that has significant contributions from the sulfur π orbitals of the ligands. Hyperfine couplings to the ^{61}Ni were interpreted as involving a spin density of 25−50% in a Ni d_{yz} orbital.[6,12,13] Schmitt and Maki reported hyperfine satellites

[†] Northwestern University.
[‡] University of Massachusetts.
[§] Current address: Department of Chemistry, Wichita State University, Wichita, KS 67260-0051.

(1) Dixon, N. E.; Gazzola, C.; Blakeley, R. L.; Zerner, B. *J. Am. Chem. Soc.* **1975**, *97*, 4131−4133.
(2) Jaun, B. *Chimia* **1994**, *48*, 50−55.
(3) Ferry, J. G. *Annu. Rev. Microbiol* **1995**, *49*, 305−333.
(4) Volbeda, A.; Garcin, E.; Piras, C.; de Lacey, A. L.; Fernandez, V. M.; Hatchikian, E. C.; Frey, M.; Fontecilla-Camps, J. C. *J. Am. Chem. Soc.* **1996**, *118*, 12989−12996.
(5) Gu, Z.; Dong, J.; Allan, C. B.; Choudhury, S. B.; Franco, R.; Moura, J. J. G.; Moura, I.; LeGall, J.; Przybyla, A. E.; Roseboom, W. R.; Albracht, S. P. J.; Axley, M. J.; Scott, R. A.; Maroney, M. J. *J. Am. Chem. Soc.* **1996**, *118*, 11155−11165.
(6) Maki, A. H.; Edelstein, N.; Davison, A.; Holm, R. H. *J. Am. Chem. Soc.* **1964**, *86*, 4580−4587.
(7) Sano, M.; Adachi, H.; Yamatera, H. *Bull. Chem. Soc. Jpn.* **1981**, *54*, 2636−2641.
(8) Schrauzer, G. N.; Mayweg, V. P. *J. Am. Chem. Soc.* **1965**, *87*, 3585−3592.
(9) Schrauzer, G. N.; Rabinowitz, H. N. *J. Am. Chem. Soc.* **1968**, *90*, 4297−4302.
(10) Schrauzer, G. N. *Acc. Chem. Res.* **1969**, *2*, 72−80.
(11) McCleverty, J. A. In *Metal 1,2-Dithiolene and Related Complexes*; McCleverty, J. A., Ed.; Interscience Publishers: New York, 1968; Vol. 10, pp 41−221.
(12) Davison, A.; Edelstein, N.; Holm, R. H.; Maki, A. H. *J. Am. Chem. Soc.* **1963**, *85*, 2029−2030.

S0020-1669(97)00363-7 CCC: $15.00
Published on Web 02/25/1998

from natural-abundance ^{33}S.[14] Depending on whether the ^{33}S parallel and perpendicular hyperfine coupling values were chosen to have the same or opposite signs, the results give 50−80% of the total spin density on the four ligand sulfur atoms. In a separate study, Heuer et al., in 1985,[15] assumed that the measured parallel and perpendicular ^{77}Se hyperfine coupling constants for bis((trifluoromethyl)ethylenediselenolato)nickelate-(III) ($[Ni(tds)_2]^-$) had the opposite sign and concluded that ∼70% unpaired spin resides on the four Se.[16]

None of these studies directly probed the spin density outside the $[NiX_4]^-$ (X = S, Se) core. However, a discrete-variational Xα molecular orbital calculation by Sano et al.[7] indicated that the olefinic carbon atoms play a significant role in the electronic ground state of the molecule by contributing between 13 and 20% of the unpaired electron spin density. We here use ENDOR and ESEEM[17−20] of ^{13}C and $^{14,15}N$ isotopomers of $[Ni(mnt)_2]^-$ to experimentally determine the spin density on the olefinic (C1) and cyano (C2) carbons and at the nitrogen (see **1a**). In a companion study, we examine the fluorine ENDOR on $[Ni(tfd)_2]^-$ (**1b**). These experiments, along with the earlier results of Maki and co-workers[6,14] and Heuer et al.,[15] regarding the $[NiX_4]^-$ core, lead to a complete description of the π spin densities on every atom of $[Ni(mnt)_2]^-$ and $[Ni(tfd)_2]^-$. These are compared with extended Hückel[21] and density functional (BLYP[22−24]) MO[25] calculations, as well as with molecular orbital calculations reported earlier.[7−10]

Experimental Section

ENDOR and ESEEM spectra were taken at either 2 or 4 K on frozen glasses, either DMSO/chloroform (1:1) or DMSO/dichloromethane (1:1), in X- and Q-band pulsed spectrometers described previously.[26,27] ENDOR frequencies are given to first order by

$$\nu_{\pm}(m) = \left|\nu_n \pm \frac{A_n}{2} + \frac{3P_n}{2}(2m-1)\right| \quad (1)$$

The peaks are centered at ν_n (nuclear Larmor frequency) and split by the hyperfine interaction, A, when A is small ($A/2 < \nu_n$) or centered at $A/2$ and split by $2\nu_n$. Additional quadrupolar interactions ($3P_n$) are present for nuclei with spin greater than $^1/_2$, and the observed splitting in the spectrum corresponds to $3P_n$ ($I \geq m > -I+1$). For comparison of spectra from ^{14}N ($I = 1$) and ^{15}N ($I = ^1/_2$) the coupling constants are related by the ratio of their Larmor frequencies (nuclear g factor)

$$\frac{A_{^{15}N}}{A_{^{14}N}} = \frac{\nu_{^{15}N}}{\nu_{^{14}N}} = 1.403 \quad (2)$$

When the quadrupolar couplings are large in comparison with the hyperfine coupling, second-order quadrupolar shifts are important and it is necessary to use the exact solution of the Hamiltonian within each m_s manifold.[28] ENDOR simulations with this solution were done using the program GENDOR run on a PC.[29,30] Pulsed ENDOR spectra were collected by use of both the Davies sequence ($\pi-T-\pi/2-\tau-\pi$)[31] and the Mims sequence ($\pi/2-\tau-\pi/2-T-\pi/2$).[32,33] The ENDOR response for the Mims sequence is a function of the product of the time between the first two pulses (τ) and the hyperfine coupling (A):

$$R = [1 - \cos(2\pi A\tau)]/2 \quad (3)$$

The response factor (R) can be optimized for a specific A, by setting τ (μs) = 1/(2nA (MHz)); it can be nulled, suppressing the response and creating a "hole" in the observed spectrum, when $\tau = 1/(nA)$. Stimulated echo ($\pi/2-\tau-\pi/2-T-\pi/2$) ESEEM time-domain spectra were Fourier-transformed into the frequency domain according to the "dead time reconstruction" method described by Mims.[34] Frequency-domain ESEEM spectra are simulated using a MatLab program created by Dr. Hong-In Lee.[35,36]

Molecular Orbital Calculations. Extended Hückel molecular orbital calculations (EHMO) were done using the program CACAO[21] and the BLYP MO calculation was performed with the Gaussian 94[25] suite of programs running on a Silicon Graphics Indigo 2 extreme computer. The LANL2DZ basis set[37] was chosen for the latter calculation because of its use of effective core potentials (ECP) to model core electrons of transition metals such as Ni, and the double-ζ basis for the valence electrons represents a good compromise between computational speed and accuracy. The coordinates for these calculations were generated using a symmetry-optimized molecule (D_{2h}) in which bond lengths and angles calculated from the crystal structure[38] were averaged.[39]

Syntheses of Ligands and Complexes. All the isotopically labeled and unlabeled samples of maleonitriledithiolate, mnt^{2-}, were synthesized by adapting the procedure of Davison et al.[40] to a small scale. *N*,*N*-Dimethylformamide (Fisher Scientific) was dried over 4 Å molecular sieves, distilled under N_2, and subsequently used as the reaction solvent. Commercially available anhydrous diethyl ether (Fisher Scientific) and isobutanol (Aldrich) were used without further purification. $K^{13}CN$ (90% ^{13}C), $KC^{15}N$ (98+%^{15}N) and $^{13}CS_2$ (99% ^{13}C) were obtained from Cambridge Isotope Laboratories. These isotopically labeled starting materials were used as obtained in the syntheses of specifically labeled samples of mnt^{2-}.

(13) Davison, A.; Edelstein, N.; Holm, R. H.; Maki, A. H. *Inorg. Chem.* **1963**, *2*, 1227−1232.
(14) Schmitt, R. D.; H., M. A. *J. Am. Chem. Soc.* **1968**, *90*, 2288−2292.
(15) Heuer, W. B.; True, A. E.; Sweptson, P. N.; Hoffman, B. M. *Inorg. Chem.* **1988**, *27*, 1474−1482.
(16) Structure **1b** with selenium replacing the sulfurs.
(17) For ENDOR and ESEEM reviews, see refs 18−20.
(18) Feher, G. *Electron Paramagnetic Resonance with Applications to Selected Problems in Biology*; Gordon & Breach: New York, 1970.
(19) Hoff, A. J. *Advanced EPR: Applications in Biology and Biochemistry*; Elsevier: Amsterdam, 1992.
(20) Abragam, A.; Bleaney, B. *Electron Paramagnetic Resonance of Transition Metal Ions*; Clarendon: Oxford, U.K., 1970.
(21) Mealli, C.; Proserpio, D. M. *J. Chem. Educ.* **1990**, *67*, 399−402.
(22) Becke, A. D. *Phys. Rev. A* **1988**, *38*, 3098−3100.
(23) Lee, C.; Yang, W.; Parr, R. G. *Phys. Rev. B* **1988**, *38*, 785−789.
(24) Miehlich, B.; Savin, A.; Stoll, H.; Preuss, H. *Chem. Phys. Lett.* **1989**, *157*, 200−206.
(25) Frisch, M. J.; Trucks, G. W.; Schlegel, H. B.; Gill, P. M. W.; Johnson, B. G.; Robb, M. A.; Cheeseman, J. R.; Keith, T.; Peterson, G. A.; Montgomery, J. A.; Raghavachari, K.; Al-Laham, M. A.; Zakrzewski, V. G.; Ortiz, J. v.; Foreman, J. B.; Cioslowski, J.; Stefanov, B. B.; Nanayakara, A.; Challacombe, M.; Peng, C. Y.; Ayala, P. Y.; Chen, W.; Wong, M. W.; Andres, J. L.; Replogle, E. S.; Gomperts, R.; Martin, R. L.; Fox, D. J.; Binkley, J. S.; Defrees, D. J.; Baker, J.; Stewart, J. P.; Head-Gordon, M.; Gonzalez, C.; Pople, J. A. *Gaussian 94*; Gaussian, Inc.: Pittsburgh, PA, 1995.
(26) Fan, C.; Doan, P. E.; Davoust, C. E.; Hoffman, B. M. *J. Magn. Reson.* **1992**, *98*, 62−72.
(27) Davoust, C. E.; Doan, P. E.; Hoffman, B. M. *J. Magn. Reson.* **1996**, *A119*, 38−44.
(28) Muha, G. M. *J. Chem. Phys.* **1980**, *73*, 4139−4140.
(29) Hoffman, B. M.; Martinsen, J.; Venters, R. A. *J. Magn. Reson.* **1984**, *59*, 110−123.
(30) Gurbiel, R. J.; Fann, Y. C.; Surerus, K. K.; Werst, M. M.; Musser, S. M.; Doan, P. E.; Chan, S. I.; Fee, J. A.; Hoffman, B. M. *J. Am. Chem. Soc.* **1993**, *115*, 10888−10894.
(31) Davies, E. R. *Phys. Lett.* **1974**, *47A*, 1−2.
(32) Mims, W. B. *Proc. R. Soc. London A* **1965**, *283*, 452−457.
(33) Gemperle, C.; Schweiger, A. *Chem. Rev.* **1991**, *91*, 1481−1505.
(34) Mims, W. B. *J. Magn. Reson.* **1984**, *59*, 291−306.
(35) The frequency domain ESEEM spectra and ENDOR peak positions were simulated using a MatLab program based on the method of Mims developed by Dr. Hong In Lee (to be published).
(36) Mims, W. B. *Phys. Rev.* **1972**, *B5*, 2409−2419.
(37) Hay, P. J.; Wadt, W. R. *J. Chem. Phys.* **1985**, *82*, 299−310.
(38) Kobayashi, A.; Sasaki, Y. *Bull. Chem. Soc. Jpn.* **1977**, *50*, 2650−2656.
(39) Bond lengths used (Å): Ni−S = 2.15, S−C(1) = 1.72, C(1)−C(1) = 1.37, C(1)−C(2) = 1.44, C(2)−N = 1.13. Bond angles used (deg): bidentate S−Ni−S = 92.5, Ni−S−C(1) = 103, S−C(1)−C(1) = 120, C(1)−C(1)−C(2) = 121, C(1)−C(2)−N = 179.
(40) Davison, A.; Holm, R. H. *Inorg. Synth.* **1967**, *10*, 8−26.

A sample of Na_2(mnt) with labeled olefinic C atoms (C1) was prepared by using $^{13}CS_2$ in the synthesis of the ligand. [^{13}C]Carbon disulfide (500 mg, 6.49 mmol) was added dropwise to a stirred suspension of finely ground dry sodium cyanide (318 mg, 6.49 mmol) in 2 mL of *N*,*N*-dimethylformamide. When the addition was complete, the reaction mixture was stirred vigorously for 30 min, during which a red-brown solid mass was produced. Isobutanol (5 mL) was added, and the mixture was heated to dissolve the product. The dark brown solution was filtered hot, and then the filtrate was cooled in an ice−salt bath; a tan crystalline solid was isolated and washed with anhydrous diethyl ether until the washings were pale yellow. The solid was then dissolved in distilled water (15 mL) and the dark brown solution rapidly lightened with the precipitation of sulfur. After 24 h, the mixture was filtered and the filtrate was evaporated to dryness under reduced pressure by use of a rotary evaporator. The yellow-brown solid thus obtained was dissolved in a minimum volume of ethanol, and the mixture was filtered to remove any undissolved material. Addition of anhydrous diethyl ether and subsequent cooling of the solution in a refrigerator yielded the ligand as a pale yellow microcrystalline solid, which was then filtered off and dried over P_4O_{10} under vacuum. Yield = 0.274 g (45% based on NaCN).

Similarly, samples of K_2(mnt) with labeled cyano C atoms (C2) were prepared by using K^{13}CN in the preparation. Carbon disulfide (667 mg, 7.577 mmol) was added dropwise to a stirred suspension of finely ground dry K^{13}CN (500 mg, 7.576 mmol) in 2 mL of *N*,*N*-dimethylformamide. Following the procedure outlined above yielded the potassium salt of the ligand as a pale yellow microcrystalline solid, which was collected by filtration and dried over P_4O_{10} under vacuum. Yield = 0.225 g (27%).

Labeling of the N atoms of the ligand was achieved by employing KC^{15}N in the synthesis. Carbon disulfide (667 mg, 7.577 mmol) was added dropwise to a stirred suspension of finely ground dry KC^{15}N (500 mg, 7.576 mmol) in 2 mL of *N*,*N*-dimethylformamide. Following the procedure outlined above yielded K_2([^{15}N]mnt) as a pale yellow microcrystalline solid which was collected by filtration and dried over P_4O_{10} under vacuum. Yield = 0.233 g (28%).

Yields of the ligands labeled in the cyano group were lower (27−28% based on KCN) than obtained for unlabeled or C1-labeled samples due to the use of KCN instead of NaCN in the synthesis, as noted in the published procedure.[40]

Syntheses of the Ni(II) complexes, $(Bu_4N)_2[Ni^{II}(mnt)_2]$, were performed as previously described[40] by the addition of an aqueous solution of $NiCl_2{\cdot}6H_2O$ (Fisher Scientific) to an ethanol−water (1:1 v/v) solution of K_2(mnt) or Na_2(mnt), followed by precipitation with Bu_4N(Br) (Aldrich).

The formally trivalent nickel complexes, $Bu_4N[Ni^{III}(mnt)_2]$, were synthesized by oxidizing the corresponding $(Bu_4N)_2[Ni^{II}(mnt)_2]$ complexes with iodine as described in the literature.[40] Samples prepared in this manner were purified by dissolving them in acetone and reprecipitating them with dry diethyl ether. The samples were collected by filtration and dried over P_4O_{10} under vacuum. Sample purity was determined by elemental analysis performed by the University of Massachusetts Microanalysis Laboratory. For unlabeled $Bu_4N[Ni^{III}(mnt)_2]$, yield = 441.5 mg (62%). Anal. Calc for $C_{24}H_{36}N_5S_4Ni$: C, 49.57; H, 6.24; N, 12.04. Found: C, 49.23; H, 6.02; N, 11.88. For [^{13}C1]$Bu_4N[Ni^{III}(mnt)_2]$, yield = 247 mg (58%). Anal. Calc for $^{13}C_4C_{20}H_{36}N_5S_4Ni$: C, 49.91; H, 6.20; N, 11.96. Found: C, 49.64; H, 6.11; N, 11.62. For [^{13}C2]$Bu_4N[Ni^{III}(mnt)_2]$, yield = 179.6 mg (60%). Anal. Calc for $^{13}C_4C_{20}H_{36}N_5S_4Ni$: C, 49.91; H, 6.20; N, 11.96. Found: C, 49.57; H, 6.07; N, 11.59. For [^{15}N]$Bu_4N[Ni^{III}(mnt)_2]$, yield = 192.2 mg (62%). Anal. Calc for $C_{24}H_{36}{}^{15}N_4NS_4Ni$: C, 49.23; H, 6.20; N, 12.64. Found: C, 49.08; H, 6.13; N, 12.46.

$[Ni(tfd)_2]^-$ was synthesized according to the procedure described by Heuer et al.[15]

Results

The EPR spectrum of $[Ni(mnt)_2]^-$ ^{13}C1-labeled at 2 K in a frozen solution (1:1 DMSO/$CHCl_3$ glass) is shown to the far right in Figure 1. The g values, $g_x = 2.14$ (x axis), $g_y = 2.04$ (y axis), and $g_z = 1.99$ (z axis), agree with those previously reported by Maki et al.[6] (the g axes and molecular axes are shown in structure **1**). Labeling with ^{13}C and ^{15}N does not broaden the EPR. $Ni(tfd)_2^-$ (**1b**) has a similar frozen-solution EPR signal and the same g values.

^{13}C1 ENDOR. Mims pulsed 35 GHz ^{13}C ENDOR spectra taken across the EPR envelope of ^{13}C1-labeled $[Ni(mnt)_2]^-$ are shown on the left in Figure 1. The interval, τ, between the first and second microwave pulses for the Mims pulse sequence, was set to maximize the ENDOR response for $A \approx 3$ MHz (τ = 144−184 ns). The top trace, taken at the high-field edge of the EPR spectrum, $g = 1.99$ (Figure 1A), is associated with molecules where the field (B_0) lies along the z axis, normal to the molecular plane (g_z). It shows a doublet centered at the ^{13}C nuclear Larmor frequency ($\nu(^{13}C) = 12.9$ MHz at 12 000 G) and split by the hyperfine coupling of $A(^{13}C1) \approx 3.0$ MHz. As the field is decreased from the edge of the EPR envelope, the breadth of the pattern decreases to $A(^{13}C1) \approx 1.5$ MHz at g = 2.01 (Figure 1C) and then increases again to $A(^{13}C1) \approx 4.6$ MHz as the field is decreased to g_y (Figure 1D−F). Continuing on to the other edge of the EPR envelope (g_x), the breadth of the pattern remains constant. However, a shoulder appears for intermediate fields, $g_y < g < g_x$ (Figure 1F,G). The spectrum taken at the g_x edge of the EPR envelope shows a sharp doublet with $A(^{13}C1) \approx 4.2$ MHz (Figure 1I). Q-band CW ^{13}C1 ENDOR measurements are of lower resolution but confirm these pulsed ENDOR results (data not shown).

The full 2-D pattern of frequency versus g can be simulated by an axial hyperfine coupling tensor that is coaxial with the **g** tensor with $\mathbf{A}[x,y,z] = +[4.6, 4.6, -3.0]$; this corresponds to an isotropic coupling $a_{iso} = -2.1$ MHz and an anisotropic dipolar tensor $\mathbf{T} = [-2.5, -2.5, 5]$ MHz. The simulations, which include the Mims response factor (eq 3), are shown below the experimental data and reproduce both the frequencies and shapes quite well, with the proviso that the ENDOR line width is deliberately set low to accentuate the features. To clarify the 2-D behavior, the figure in the center of Figure 1 shows a plot of peak positions versus g values; the shaded region identifies responses suppressed by the choice of τ. The relative signs of the hyperfine couplings are determined by the simulation; the absolute signs are fixed by assuming that the dipolar contribution to the C1 hyperfine tensor comes from spin density in the $2p_z$ orbital on C1 ($\rho(^{13}C1)_{2p_z}$) that arises from delocalization of the odd-electron orbital. Comparison of the measured dipolar component along g_z ($T = 5$ MHz) to that for a single spin in $2p_z$, $T_{\rho=1}(^{13}C) = 184$ MHz, gives $\rho(^{13}C1)_{2p_z} = T/T_{\rho=1}(^{13}C) = 0.025$.

^{13}C2 ENDOR. Pulsed and CW ^{13}C ENDOR spectra of $[Ni(mnt)_2]^-$ labeled with ^{13}C at the cyano carbons (C2) agree in showing one doublet at all fields across the EPR envelope (data not shown). The splitting decreases from $A \sim 3.4$ MHz at the high-field edge (g_z) of the envelope, to $A \sim 2.6$ at g_x. This is consistent with a hyperfine tensor that differs qualitatively from that of C1 in being largely isotropic, $\mathbf{A}(^{13}C2) = [2.6, 2.8, 3.4]$ MHz, corresponding to $\mathbf{T} = [0.17, 0.27, -0.43]$ MHz and $a_{iso} = -2.9$ MHz. The small dipolar component corresponds π spin density of less than 0.5%.

^{14}N ENDOR. The CW (data not shown) and Mims pulsed ^{14}N ENDOR spectra taken at g_z (Figure 2A) show a doublet of doublets, as expected from eq 2. This pattern can be assigned in either of two ways: $A(^{14}N) = 0.94$ MHz with a quadrupole splitting of $3P = 2.4$ MHz or $A(^{14}N) = 2.4$ MHz with a quadrupole splitting of $3P = 0.94$ MHz. The key to distinguishing is to note that the spectrum is centered not exactly at ν_N ($\nu(^{14}N) = 3.7$ MHz at 12 000 G) but rather at a frequency

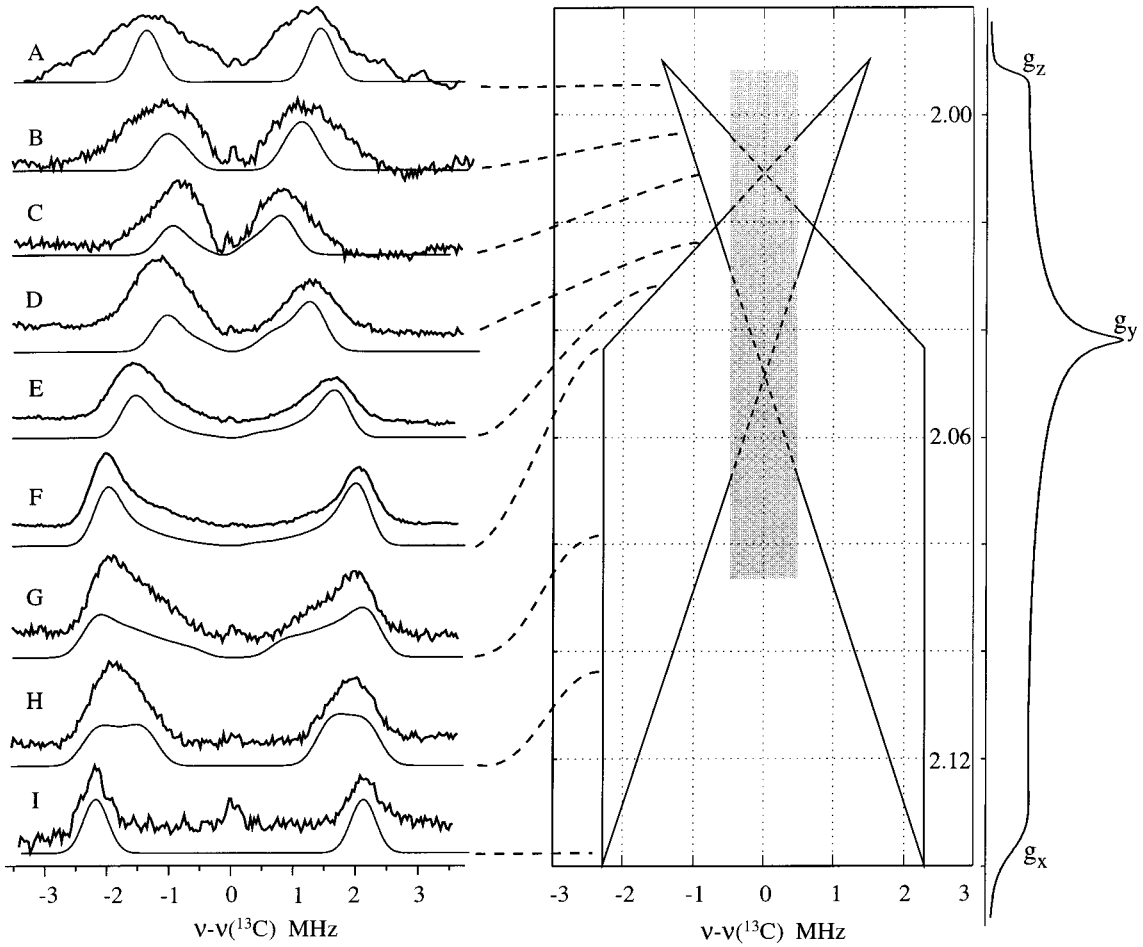

Figure 1. ^{13}C1 Mims ENDOR of $[Ni(mnt)_2]^-$ is shown at left of the figure with simulations shown below. To the right is a scheme which maps out the hyperfine tensor. Between the two figures are dashed lines which connect the spectra and simulations to the position on the peaks in the scheme. At the far right is the 2 K dispersion mode CW EPR spectrum of ^{13}C1-labeled $[Ni(mnt)_2]^-$ with the g values marked. The shaded area on the scheme shows the peaks that are suppressed due to the choice of τ. Pulse conditions: microwave frequency 34.702 GHz; $T = 2$ K; $t_{RF} = 60$ μs; $\pi/2$ pulse width 32 ns; repetition rate 71 Hz; number of scans (A, C, I) 1 scan, (B, D, G, H) 4 scans, (E, F) 7 scans; (A, C−I) $\tau = 144$ ns, (B) $\tau = 164$ ns; field (A) 12 440 G, (B) 12 380 G, (C) 12 350 G, (D) 12 230 G, (E) 12 180 G, (F) 12 136 G, (G) 12 000 G, (H) 11 800 G, (I) 11 858 G. Pulse simulation conditions: Simulations were done using GENDOR using the parameters discussed in the text. The simulations were then multiplied by the response factor for the appropriate choice of τ. The scheme was generated using a Matlab program. EPR conditions: microwave frequency 35.25 GHz, modulation amplitude 0.67 G, time constant 32 ms, modulation frequency 100 kHz, power 0.2 mW.

0.3 MHz greater than $\nu(^{14}N)$. Such an offset arises from the "second-order" effects of a quadrupole coupling that is large compared to the hyperfine coupling, and thus the offset indicates the former assignment. To confirm this, simulations were done with both sets of hyperfine and quadrupole parameters: only the simulation that uses the parameters with the large quadrupole ($3P = 2.4$ MHz) (Figure 2B) matches the experimental spectrum's frequencies and relative intensities. Furthermore, the value $\tau = 380$ ns in the Mims pulsed spectrum was chosen to optimize the response for $A \sim 1$ MHz (eq 3) and would have suppressed signals where $A = 2.6$ MHz, contrary to observation.

^{15}N ENDOR and ^{14}N ESEEM. Because ^{14}N ENDOR was not easily obtained at g values other than g_z, the molecule was isotopically enriched with ^{15}N to determine the full ^{14}N hyperfine tensor. ^{14}N ESEEM of natural-abundance $[Ni(mnt)_2]^-$ was then used to obtain the ^{14}N quadrupole tensor.

Figure 3 shows the field dependence of the ^{15}N Mims pulsed ENDOR spectra. The spectrum taken at g_z corresponds to $A(^{15}N) = 1.3$ MHz, as predicted by eq 2 from the measured value, $A(^{14}N) = 0.94$ MHz, thus confirming the above ^{14}N assignment. The field dependence of the ^{15}N Mims ENDOR spectra is characteristic of an approximately axial dipolar hyperfine splitting with the largest component along the g_z axis.

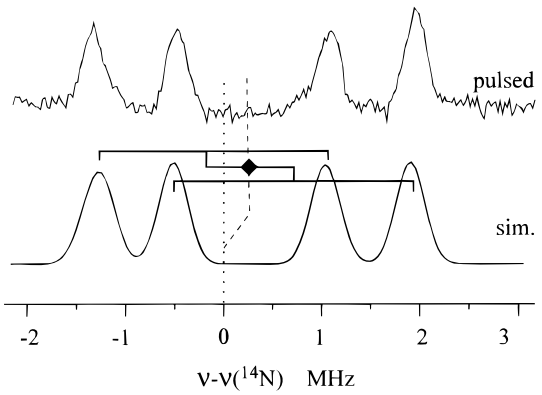

Figure 2. ^{14}N Mims ENDOR of $[Ni(mnt)_2]^-$ with simulation at g_z. Pulse conditions: microwave frequency 34.76 GHz, $T = 2$ K, $\pi/2$ pulse width 60 ns, $t_{RF} = 60$ μs, $\tau = 380$ ns, repetition rate 50 Hz, field 12 450 G, 6 scans. Simulation was done using GENDOR, $\theta = \phi = 0°$, $\alpha = 60°$, $\beta = 90°$, and $\gamma = 0°$, ENDOR line width 0.2 MHz $\mathbf{A}_{x,y,z} = [0.13, 0.10, 0.94]$ MHz, and $\mathbf{P}_{x,y,z} = [0.85, 1.1, -1.95$ MHz]. Horizontal brackets represent the quadrupole couplings; the breadth of the zigzag line is the hyperfine coupling. The dotted line is at $\nu(^{14}N)$, and the dashed line through ◆ shows the offset discussed in the text.

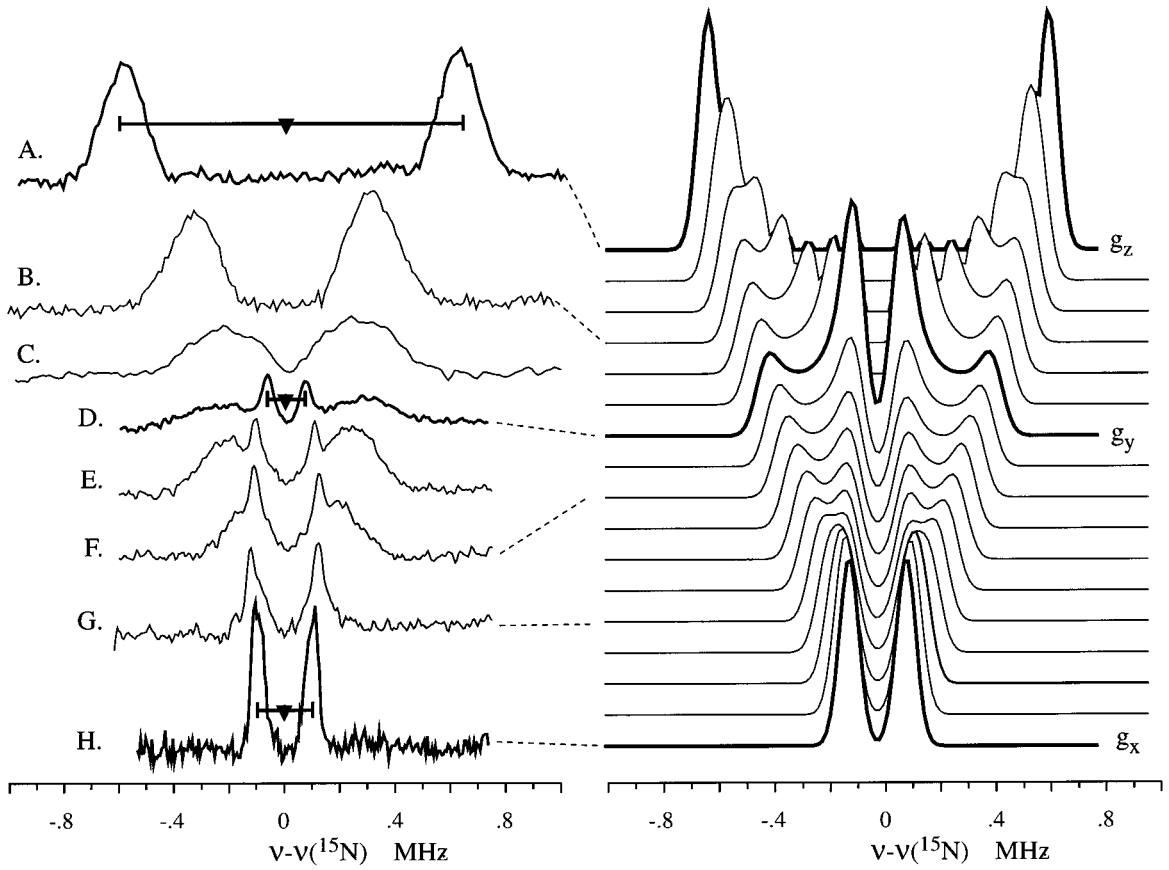

Figure 3. ^{15}N Mims pulsed ENDOR (left) and simulations (right). Conditions (left): microwave frequency 34.83 GHz; $T = 2$ K; $\pi/2$ pulse width 60 ns; $t_{RF} = 60$ μs; repetition rate 25 Hz; (A) $\tau = 1.152$ μs, (B−H) $\tau = 800$ ns; field (A) 12 450 G, (B) 12 330 G, (C) 12 230 G, (D) 12 190 G, (E) 12 110 G, (F) 11 960 G, (G) 11 860 G, (H) 11 660 G; number of scans (A, C) 4, (B) 2, (D, G, H) 1, (E) 6, (F) 3. Conditions (right): simulations using GENDOR, with $\theta = \phi = 0°$, ENDOR line width 0.02 MHz, $\mathbf{A}_{x,y,z} = [0.20, 0.15, 1.3]$ MHz. g_x, g_y, and g_z are in bold in both the experimental spectra and the simulations. Brackets in spectra represent measured hyperfine couplings and ▼ designates ν(^{15}N).

Simulations of the data using an essentially axial hyperfine tensor of $\mathbf{A}_{x,y,z} = [0.2, 0.16, 1.30]$ MHz, corresponding to $\mathbf{T}_{x,y,z} = [-0.35, -0.39, 0.75]$ MHz and $a_{iso} = 0.55$ MHz, agree with the data well (see figure at right).

Figure 4 shows the time domain and frequency domain Mims X-band ESEEM spectra of ^{14}N natural-abundance $[Ni(mnt)_2]^-$ taken with $\tau = 140$ ns to suppress modulation from protons in either the solvent or counterion. At g_z, the ^{14}N modulation is deep (Figure 4A), and frequency domain, Figure 4D, shows three distinct peaks between 2.8 and 4.5 MHz, along with weak low-frequency peaks. Moving away from this g value, the modulation depth decreases dramatically as seen in Figure 4B,C. The transform of the g_y time wave (Figure 4E) shows a splitting of the higher frequency peaks, while that of g_x (Figure 4F) shows only two peaks. The frequency domain spectra were simulated using a ^{14}N hyperfine coupling tensor obtained by scaling that determined by the ^{15}N ENDOR. A cyano group nitrogen is expected to have a nearly axial quadrupolar coupling tensor, $\mathbf{P}_{1,2,3} = [-P_{||}/2, -P_{||}/2, P_{||}]$, with $P_{||}$ along the bond ($3P$ is the measured quadrupole coupling), which lies in the molecule at an angle of 60° with g_x; the other components are perpendicular to the CN bond, one in the plane of the molecule and the other perpendicular to the plane (along g_z). In this case, the quadrupole splitting measured in the ^{14}N ENDOR spectrum at g_z (Figure 2A) corresponds to $P_{||}/2$, and this gave an initial estimate of $e^2qQ = 2P_{||} \sim 4$ MHz. The final simulations, shown below the experimental figures, used the parameters $e^2Qq = 3.9$ MHz and a slight rhombicity, $\mathbf{P}_{1,2,3} = [2.4, 2.6, 5.0]$ MHz, with the out-of-plane component, P_1, as the smallest. The

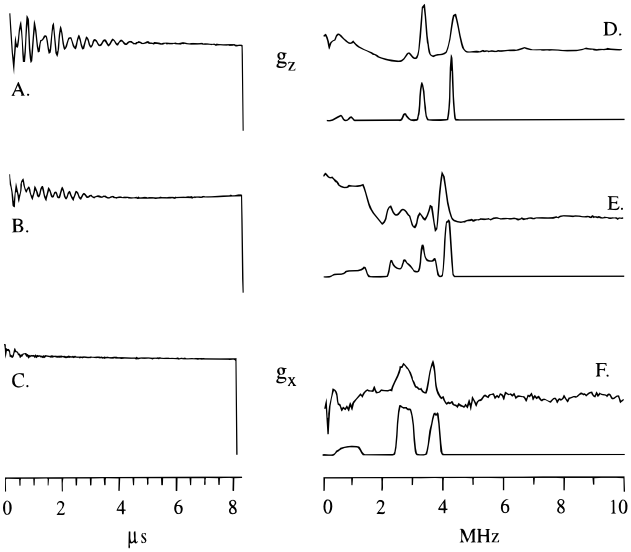

Figure 4. ^{14}N ESEEM of $[Ni(mnt)_2]^-$ shown in the time domain (A−C) and in the frequency domain with simulations (D−F). ESEEM conditions: microwave frequency 9.70 GHz; $T = 4$ K; repetition rate 33 Hz; $\tau = 140$ ns; $t_p = 16$ ns; field (A) 3480, (B) 3430, (C) 3240 G; number of scans (A) 3, (B) 12, (C) 10. Fourier transforms (D−F) of the time domain were obtained by dead time reconstruction patterned after Mims.[34] Simulations of the frequency domain were done using a MatLab program and are shown below the experimental spectra. Conditions: $\theta = \phi = 0°$, $\alpha = 60°$, $\beta = 90°$, and $\gamma = 0°$, $\mathbf{A}_{x,y,z} = [0.13, 0.10, 0.94]$ MHz, $e^2qQ = 3.9$ MHz, and $\eta = 0.15$.

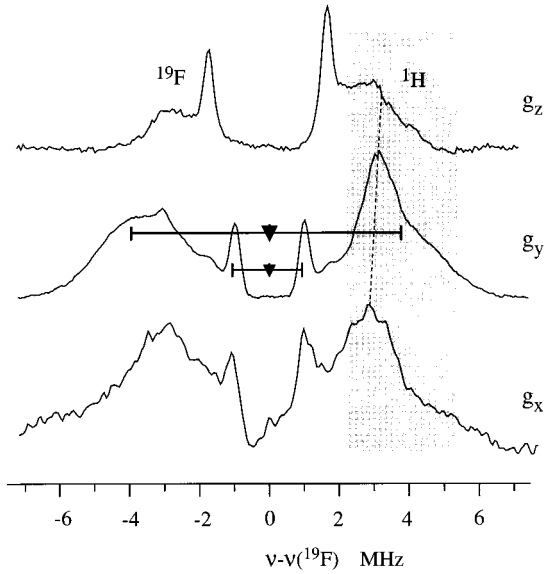

Figure 5. ^{19}F Davies ENDOR at g_x, g_y, and g_z. Conditions: microwave frequency 34.68 GHz; $T = 2$ K; $\pi/2$ pulse width 132 ns; $t_{RF} = 60$ μs; $\tau = 510$ ns; repetition rate 42 Hz; field (g_x) 11 550 G, (g_y) 12 130 G, (g_z) 12 440 G; number of scans (g_x) 8, (g_y) 3, (g_z) 4. Brackets in the g_y spectrum represent measured hyperfine couplings and ▼ designates ν(^{19}F). The shaded area is dominated by ν(^{1}H) as stated in the text.

ESEEM frequency domain spectra (Figure 4D,E,F) are reproduced quite nicely with these parameters. The agreement between the ^{15,14}N ENDOR and ESEEM spectra confirms the analysis of both the hyperfine and quadrupole tensors. Consideration of these ^{14,15}N tensors shows that the difficulty in obtaining the ^{14}N ENDOR spectra at g_x and g_y arose because of the combination of extremely small hyperfine values and large quadrupolar couplings. The spin density in the ^{14}N $2p_z$ orbital is calculated using the scaled dipolar contribution component of $A(^{14}N)$, $\mathbf{T}(^{14}N) = [-0.26, -0.29, 0.55]$ MHz: $\rho(^{14}N)_{2p_z} = T_3/T_{\rho=1}(^{14}N) = 0.01$ ($T_{\rho=1}(^{14}N) = 96$ MHz).

^{19}F ENDOR of [Ni(tfd)$_2$]$^-$. Figure 5 shows fluorine ENDOR spectra of [Ni(tfd)$_2$]$^-$, where CF_3 has replaced the CN group (structure **1b**). ^{1}H ENDOR signals from solvent or an ion-paired tetra-*n*-butylammonium cation, centered at the proton Larmor frequency ($\nu(^{1}H) = 51.1$ MHz at 12 000 G), are shaded in the figure; overlap from the ^{1}H signal alters the intensity of the ν_+ branch of the ^{19}F signal at all fields. The ^{19}F signal at g_z shows a sharp doublet centered at the fluorine Larmor frequency ($\nu(^{19}F) = 48.3$ MHz at 12 000 G) with a hyperfine coupling of $A(^{19}F) = 3$ MHz. This rides on an unresolved, broad ^{19}F doublet with hyperfine couplings in the range $A(^{19}F) \approx 3-7$ MHz, with the most probable value at $A(^{19}F) \approx 6$ MHz. The coupling of the sharp doublet decreases to $A(^{19}F) = 2$ MHz at g_y and changes little at still lower fields ($A(^{19}F) = 2.2$ MHz at g_x). The broad coupling extends over a wider range at the higher g values, $A(^{19}F) \approx 2-11$ MHz at g_y, with $A(^{19}F) \approx 7-8$ MHz being the most probable. The ^{19}F hyperfine couplings are expected to arise from hyperconjugation with spin density in a C1 $2p_z$ orbital and to have a roughly isotropic coupling that depends on the angle θ between the C1 $2p_z$ orbital and the CF bond according to the following equation:[41]

$$A = a + b\cos^2\theta \qquad (4)$$

The broad peak is assigned to a distribution of rotamers. Taking the maximum and minimum hyperfine coupling of the broad peaks, $A(^{19}F) = 11$ and 2 MHz, respectively, gives $b = 9$ MHz and $a = 2$ MHz. The isotropic hyperfine coupling corresponds to a minuscule spin density on the fluorine ($a_{iso}(\rho = 1) = 47\,910$ MHz; $\rho(F) \sim a/a_{iso} \sim 4 \times 10^{-5}$). The sharp doublet presumably corresponds to one specific, well-populated orientation.

Table 1. Spin Densities

nuclei	ρ(exp)	ρ(Xα)[c]	ρ(BLYP)[c]	ρ(EH)[c]
^{61}Ni	0.25[a]	0.179	0.175	0.16
^{33}S	0.13[b]	0.161	0.144	0.13
[NiS$_4$]	0.85	0.82	0.75	0.68
^{13}C1	0.025	0.029	0.047	0.06
^{13}C2	0.003	0.002	0.00	0.01
^{19}F	0.000			
^{14,15}N	0.01	0.013	0.014	0.02

[a,b] Spin density reported as a range by Maki et al.[6] determined from the ^{61}Ni hyperfine and spin density for S depends on the sign the ^{33}S hyperfine coupling constant (0.13 vs 0.20)[14] as discussed in text. [c] Xα spin densities are from Sano et al.[7] EH[21] and BLYP[25] are calculated as described in the text.

MO Calculations of [Ni(mnt)$_2$]$^-$. The results of the Xα,[7] EH,[21] and BLYP[25] MO calculations are shown in Table 1; the SOMO, as calculated by the BLYP MO method, is superposed on the molecular framework of [Ni(mnt)$_2$]$^-$ in Figure 6. All agree in giving a large majority of spin to the [NiS$_4$]$^-$ core, with the Xα MO calculation, for which $\rho(NiS_4^-) = 0.82$ (Table 1), being closest to the experimental results; $\rho(NiS_4^-) = 0.85$. Looking at the individual atom spin densities, the differences between the calculated and experimental C1 and N spin densities do not appear appreciable because the individual spin densities themselves are small. However, it may be worth noting that the aggregate results for the two high-level calculations give a good representation of the total spin density on the NiS_4 core, but the EH calculation appreciably underestimates the spin on the core, $\rho(NiS_4^-) = 0.68$, and correspondingly overestimates that on the remainder of the molecule.

Discussion

We have determined the hyperfine tensors for C1, C2, and N of [Ni(mnt)$_2$]$^-$, along with the quadrupole tensor for nitrogen. The large difference between the ^{14}N quadrupole coupling constants and the hyperfine coupling constants, which causes second-order effects in the ^{14}N splitting pattern resulting in a shift to slightly higher frequencies (+0.3 MHz) of [Ni(mnt)$_2$]$^-$ at g_z, made it necessary to use both ^{14}N ESEEM and ^{15}N ENDOR to determine complete hyperfine and quadrupole tensors. However, we note that the upshift, which is accounted for in the exact solution of the Hamiltonian given by Muha,[28] can be used in other studies to assign an ENDOR pattern with large quadrupole splittings and weak hyperfine interactions. The excellent agreement of the frequency domain ESEEM spectra and ESEEM simulations based on ENDOR determinations of the quadrupolar and hyperfine coupling tensors confirms those tensors. These measurements give $\rho(C1) \sim 0.03$ in the C1 $2p_z$ orbital, as shown in Table 1, and $\rho(C2) < 0.003$. The calculated π spin density is small for nitrogen as shown in Table 1.

In total, ~0.15 of the unpaired electron resides on the ligand atoms (C and N), while the rest resides in the NiS_4 core, giving $\rho(NiS_4^-) = 0.85$. This result confirms certain assumptions made in the earlier reports of Ni and S spin densities. The spin densities reported by Maki and co-workers hinged on the relative signs of the parallel and perpendicular hyperfine coupling constants of ^{61}Ni and ^{33}S hyperfine tensor components,[6,14] as

(41) Gordy, W. *Theory and Applications of Electron Spin Resonance*; John Wiley & Sons: New York, 1980; Vol. XV.

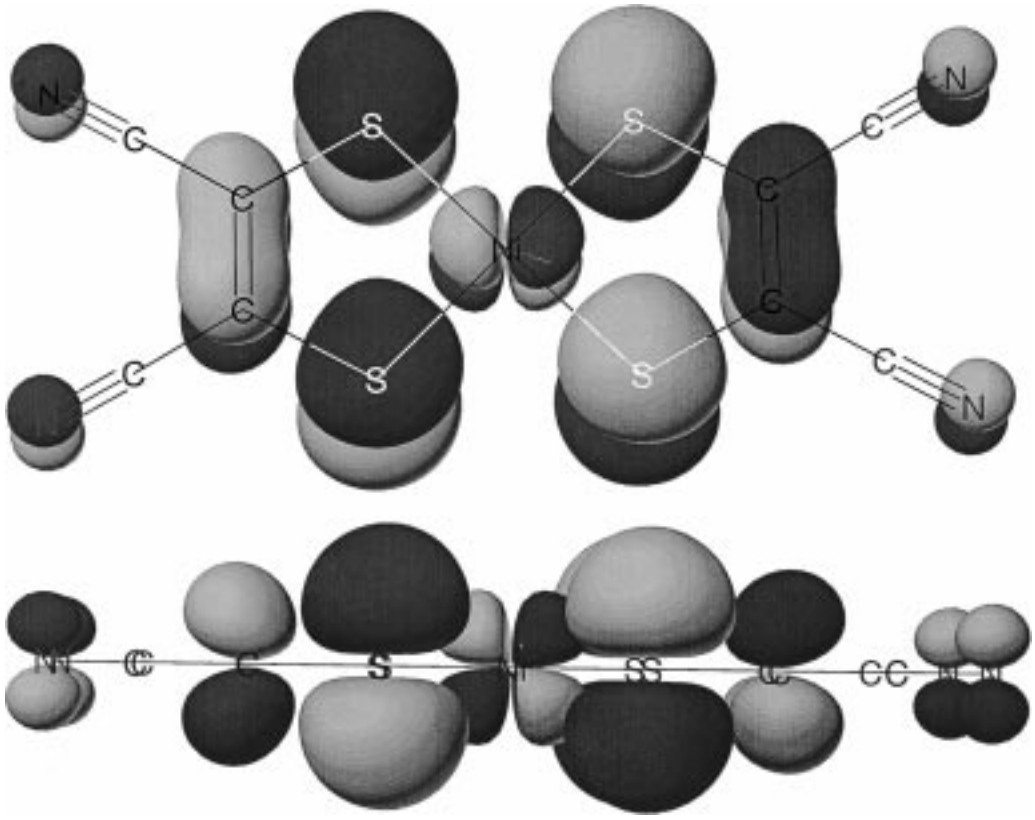

Figure 6. Diagram of the $[Ni(mnt)_2]^-$ SOMO drawn from the BLYP wave function at a value 0.03. Black and gray represent opposite signs of the wave functions. Top: view nearly along the *z* axis. Bottom: view along the *x* axis.

discussed above. An assumption of opposite signs for the dipolar hyperfine couplings of the nickel gave ρ(Ni) $\sim$ 0.25−0.50 for the unpaired electron residing on the Ni, and our measurements support the lower end of this range (0.32). The tensor components of the natural-abundance ^{33}S hyperfine satellites ($A_\perp$ and $A_{||}$) were chosen to have the same sign, which gives a total of 0.50−0.60 of the unpaired electron on the four sulfurs.[14] The total $[NiS_4]$ spin density of ∼0.85 is consistent with our results, confirming the earlier sign choices. The weak ^{19}F coupling pattern seen for $[Ni(tfd)_2]^-$ shows that the electronic structure of the compound must be similar to that of $[Ni(mnt)_2]^-$, and this supports the analysis of Heuer et al.,[15] which put ρ-$[NiSe_4]$ $\sim$ 0.85.

For comparison with experiment, we performed extended Hückel (EH) calculations[21] and BLYP MO calculations[25] to obtain predicted spin densities on C1, C2, and N, as well as S and Ni, and give these results along with those from the Xα calculation[7] in Table 1; a picture of the HOMO derived in the BLYP MO calculation is given in Figure 6. All the MO calculations, EH, Xα, and BLYP, agree with experiment in having the majority π spin density on the $[NiS_4]$ core, with most of that spin located on the four sulfurs. In absolute terms, the spin densities predicted for C and N by the three MO calculations differ little, because the ρ's are small, but the Xα agrees best with experiment. If we focus on the ρ of individual atoms, not groups, the ratio, ρ(C1)/ρ(S) $\sim$ 0.025/0.16 $\sim$ 0.16, indicates a rather substantial ability to support π delocalization from the 3p π orbital on S to the 2p π orbital on C. This can be contrasted to an analogous study by Keijzers and co-workers,[42] where ENDOR and ESEEM were used to probe the electronic structure of $[Cu(mnt)_2]^{2-}$, and the results of those experiments showed small amounts of σ delocalization through bond polarization.

The results obtained support the notion that S-donor atoms are intimately involved in the oxidative chemistry associated with Ni sites in hydrogenases and other enzymes with cysteine ligation of Ni. This provides one possible explanation for the lack of changes in electron density on Ni or in the Ni−S bond length observed for the Ni site in hydrogenase by XAS.[5] Recently, it was shown the Ni site of hydrogenase forms part of a heterodinuclear, [Ni, Fe] center.[4,43−45] Although the subject of the redox chemistry of this center is controversial, IR studies indicate that the Fe ion is not redox active.[4,44,46,47]

Acknowledgment. We thank Mr. Clark E. Davoust for expert technical assistance. This work was supported by grants from the NIH (GM-38829 (M.J.M.); HL 13531(B.M.H.); Training Grant to Northwestern University 5 T32 GM0838205 (J.E.H.)).

IC9703639

(42) Reijerse, E. J.; Thiers, A. H.; Kanters, R.; Gribnau, M. C. M.; Keijzers, C. P. *Inorg. Chem.* **1987**, *26*, 2764−2769.
(43) Volbeda, A.; Charon, M.-H.; Piras, C.; Hatchikian, E. C.; Frey, M.; Fontecilla-Camps, J. C. *Nature* **1995**, *373*, 580−587.
(44) Happe, R. P.; Roseboom, W.; Bagley, K. A.; Pierik, A. J.; Albracht, S. P. J. *Nature* **1997**, *385*, 126.
(45) Huyett, J. E.; Carepo, M.; Pamplona, A.; Franco, R.; Moura, I.; Moura, J. J. G.; Hoffman, B. M. *J. Am. Chem. Soc.* **1997**, *119*, 9291−9292.
(46) Dole, F.; Fournel, A.; Magro, V.; Hatchikian, E. C.; Bertrand, P.; Guigliarelli, B. *Biochemistry* **1997**, *36*, 7847−7854.
(47) Bagley, K. A.; Duin, E. C.; Roseboom, W.; Albracht, S. P. J.; Woodruff, W. H. *Biochemistry* **1995**, *34*, 5527−5535.